A Multiepoch X-Ray Study of the Nearby Seyfert 2 Galaxy NGC 7479: Linking Column Density Variability to the Torus Geometry

A. Pizzetti[1] , N. Torres-Albà[1] , S. Marchesi[1,2] , M. Ajello[1] , R. Silver[1] , and X. Zhao[3]
[1] Department of Physics and Astronomy, Clemson University, Kinard Lab of Physics, Clemson, SC 29634, USA; apizzet@g.clemson.edu
[2] INAF—Osservatorio di Astrofisica e Scienza dello Spazio di Bologna, Via Piero Gobetti, 93/3, I-40129, Bologna, Italy
[3] Center for Astrophysics—Harvard & Smithsonian, 60 Garden Street, Cambridge, MA 02138, USA

Abstract

Active galactic nuclei are powered by accreting supermassive black holes, surrounded by a torus of obscuring material. Recent studies have shown how the torus structure, formerly thought to be homogeneous, appears to be "patchy": the detection of variability in the line-of-sight hydrogen column density, in fact, matches the description of an obscurer with a complex structure made of clouds with different column density. In this work, we perform a multiepoch analysis of the X-ray spectra of the Seyfert 2 galaxy NGC 7479 in order to estimate its torus properties, such as the average column density and the covering factor. The measurement of the line-of-sight hydrogen column density variability of the torus allows us to obtain an upper limit on the cloud distance from the central engine. In addition, using the X-ray luminosity of the source, we estimate the Eddington ratio to be in a range of $\lambda_{\rm Edd} = 0.04$–0.05 over all epochs.

1. Introduction

Active galactic nuclei (AGN) are accreting supermassive black holes (SMBHs) at the center of galaxies, surrounded by a structure of obscuring material, which historically has been assumed to have a toroidal shape (unification model, Antonucci 1993; Urry & Padovani 1995).

Results obtained by using millimeter/submillimeter, infrared, optical, and X-ray facilities (see, e.g., Simpson 2005; Combes et al. 2019; Hönig 2019; Zhao et al. 2021) suggest the presence of a doughnut-like structure of molecular gas and dust on the 0.1–100 pc scale as the origin of the obscuration and reflection of the radiation coming from the inner part of the AGN. The shape and the size of the torus is still a matter of debate, with recent studies suggesting a warped disklike structure as a more appropriate description of the geometry of the obscuring material (Antonucci 1993; Combes et al. 2014, 2019; Audibert et al. 2019; Buchner et al. 2021). The radiation is reprocessed by the dust and the molecular gas of the torus; the dust absorbs the radiation and thermally reemits it in infrared. The thick molecular gas, instead, reprocesses the incoming radiation via photoelectric absorption and Compton scattering, generating the Compton hump feature present in the X-ray spectra of the most obscured sources.

Infrared and X-ray studies of the torus (see, e.g., Risaliti et al. 2002, 2005; Bianchi et al. 2005; Risaliti et al. 2011; Sanfrutos et al. 2013; Markowitz et al. 2014; Balokovic et al. 2018; Buchner et al. 2019; Laha et al. 2020) have ruled out the initial idea of a homogeneous torus, leaving the clumpy scenario, where the torus is made of multiple clouds of different densities, to be a more accurate description of the spatial distribution of the obscuring material. If this is indeed the case, in X-ray we should expect to see line-of-sight (LOS) hydrogen

column density ($N_{\rm H,los}$) variability on timescales that vary from days (Risaliti et al. 2005), to months (Risaliti et al. 2002), to years (Elvis et al. 2004), depending on the size of the clouds and their distance from the X-ray emitter (Risaliti et al. 2005; Nenkova et al. 2008).

Larger source samples have been considered by Markowitz et al. (2014) and Laha et al. (2020) when probing the $N_{\rm H}$ variability in Seyfert 1 and Compton-thin ($N_{\rm H,los} < 1.5 \times 10^{24}$ cm^{-2}) Seyfert 2 galaxies.[4] Both works show that eclipsing events are common among Sy2 galaxies. Nevertheless, in the sample considered by Laha et al. (2020), only only 7/20 sources show variability in the column density of the full-covering absorber, and 11/20 sources required the addition of a partial-covering obscuring component in order to better explain the observations. This suggests a scenario where clouds of different densities and radial velocities moving inside a more diffuse medium is preferred over a simple clumpy torus or the classic homogeneous doughnut-shaped torus one. These recent works reveal the torus as a complex medium, likely containing substructures, the characteristics of which can only be proved through additional $N_{\rm H}$ variability studies.

For this work, we focused on the analysis of a single source, NGC 7479, having as a main goal the characterization of the properties and the geometry of its torus. The study was done by analyzing the hydrogen column density variability via a simultaneous fit of multiepoch X-ray spectra. Previous works done by Marchesi et al. (2019) and Zhao et al. (2021) showed this galaxy to be a heavily obscured AGN (line-of-sight hydrogen column density $N_{\rm H,los} = 24.76^{+0.08}_{-0.07}$ cm^{-2}, Zhao et al. 2021) and a potential $N_{\rm H,los}$ variable AGN. As shown in Baloković et al. (2021) and Saha et al. (2022), the multiepoch X-ray spectral analysis is a powerful tool to constrain torus parameters such as

---

[4] Based on their optical spectra, Seyfert galaxies have been classified Seyfert 1, when both narrow and broad line regions are visible and Seyfert 2, when only the narrow lines are present, due to the obscuration of the torus (Antonucci 1993; Urry & Padovani 1995).
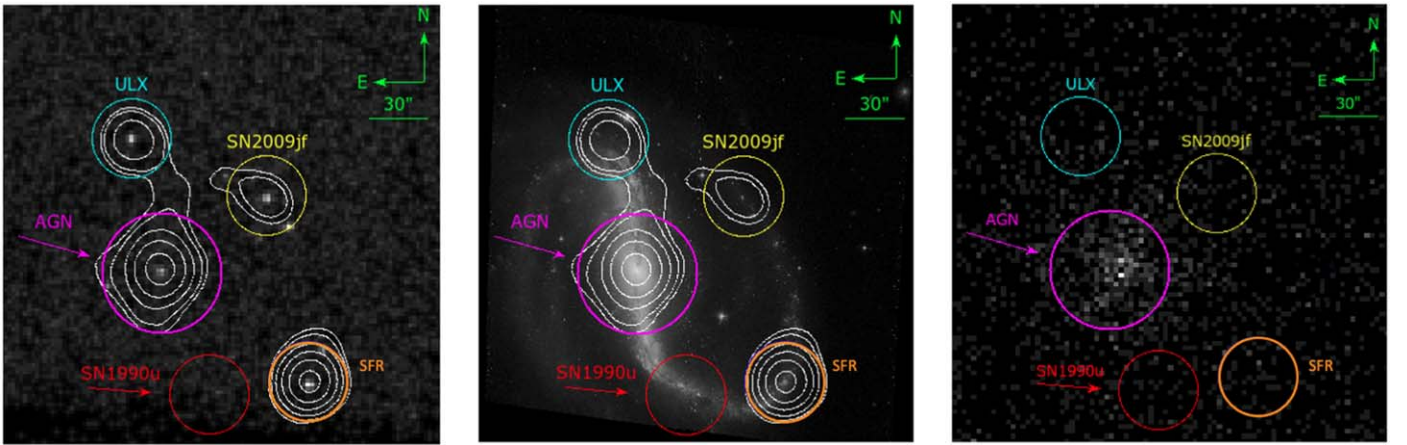
Figure 1. XMM-Newton EPIC-PN contours (white) overplotted on Chandra-b (left) and the Hubble Space Telescope (center) observation of NGC 7479. The right panel shows the NuSTAR-1 observation. In the figure, the other X-ray sources in the galaxy are also highlighted: the ultraluminous X-ray source (ULX; cyan), the star-forming region (SFR) (orange), the supernova SN 2009jf (yellow), the supernova remnant of SN 1990u (red), and the central engine (magenta). The regions showed in the figure are for display only and do not correspond to the ones used for the spectral extraction.

Table 1
Source Observation Details of NGC 7479

Instrument	ObsID	Exposure Time (ks)	Start Date
XMM-Newton-a	0025541001	5.6	2001-06-19
XMM-Newton-b	0301651201	16.0	2006-07-13
Chandra-a	10120	25.1	2009-08-11
Chandra-b	11230	10.1	2009-10-24
NuSTAR-1	60201037002	18.5	2016-05-12
XMM-Newton-c	0824450601	64.4	2018-05-30
NuSTAR-2	60061316002	23.6	2020-11-06

Note. For XMM-Newton, the reported exposure times correspond to EPIC-PN (after removing background flares). The XMM-Newton-b observation was removed due to flare contamination.

the covering factor, the torus inclination angle, the photon index, and the average hydrogen column density, while, at the same time, analyzing the $N_{H,los}$ variability.

The paper is structured as follows: in Sections 2 and 3, the data reduction and analysis is performed, as well as the description of the models used for the spectral fitting. In Section 4 we discuss the results obtained in this work and compare them to previous analysis of NGC 7479; in particular, we focus on the connection between the line-of-sight hydrogen column density variability with respect to the torus geometry. Finally, we report our conclusions in Section 5. The cosmological parameters assumed in this work are compatible with a flat ΛCDM cosmology with $H_0 = 69.6 \, \text{km s}^{-1} \, \text{Mpc}^{-1}$, $\Omega_m = 0.29$ and $\Omega_\Lambda = 0.71$ (Bennett et al. 2014). All reported uncertainties are at 90% confidence level unless otherwise stated.

2. Observations and Data Analysis

NGC 7479 ($z \sim 0.007941$, $d \sim 36$ Mpc, Haynes et al. 1998) is a Seyfert 2 galaxy (Lumsden et al. 2001) detected in the 150 month Burst Alert Telescope (BAT) catalog (K. Imam et al. in preparation.[5]); a catalog of ~ 1000 AGN detected by Swift-BAT in the 15–150 keV range. The source was selected from

---

[5] The online version of the catalog can be found at https://science.clemson.edu/ctagn/bat-150-month-catalog/.

the work of Zhao et al. (2021) because of the number and cadence of its existing observations, and because of the tentative detection of line-of-sight N_H variability in the mentioned work. The analysis of one NuSTAR (2016 May 12) and one XMM-Newton (2018 May 30) observation reported in Zhao et al. (2021), shows a $\Delta log \, N_{H,los} = 0.20^{+0.10}_{-0.08}$ between the line-of-sight column densities of the two observations, in a time span of 2.05 yr. Further public archival data are available in the 0.5–10 keV and 3–70 keV ranges for XMM-Newton/Chandra and NuSTAR, respectively. In total, NGC 7479 has two observations with Chandra, one with NuSTAR, and three with XMM-Newton. Table 1 reports the main details of the observations analyzed in this work.

NGC 7479 contains multiple X-ray sources, as can be seen in the $\sim 3' \times 3'$ region in Figure 1. The galaxy has been the host of two supernova explosions (SN1990u, Kasliwal et al. 2009 and SN2009jf, Pennypacker et al. 1990), the latest of which was detected by Chandra. The high resolution images obtained with Chandra allowed us to highlight the presence of an ultraluminous X-ray source (ULX; Voss et al. 2011), a star-forming region (Zhou et al. 2011), and the supernova SN1990u (Kasliwal et al. 2009). Figure 1—left—also shows XMM-Newton intensity contours overlaid on the Chandra-b image, which indicates that the separation between the sources is large enough to isolate the AGN from the other elements, not only in the Chandra image, but also in the XMM-Newton one. The NuSTAR images show one single source, as can be seen in Figure 1—right. To minimize any possible residual contamination, however, we limited the NuSTAR extraction radius to $30''$, same as used for XMM-Newton.

2.1. Chandra Data Reduction

For this work, we use two Chandra observations taken on 2009 August 11 and 2009 October 24, with an exposure time of ~ 25 ks and ~ 10 ks, respectively.

The data were reduced with the CIAO (v4.14; Fruscione et al. 2006) software and the Chandra calibration database `caldb` 4.9.7 adopting standard procedures. The source and the background spectra were extracted using the CIAO `specextract` tool. For the source, we selected a circle of $5''$, while the background was extracted from an annulus of internal radius $r_{in} = 6''$ and external radius $r_{out} = 15''$, after a visual

inspection to avoid the presence of any other source in the field. Due to the low exposure time, we grouped each spectrum with a minimum of 5 counts per bin with the grppha tool. Therefore, the spectra are fitted with the cstat statistics Cash ([1979]).

2.2. XMM-Newton Data Reduction

NGC 7479 has three archival XMM-Newton observations taken on 2001 June 19, 2006 July 13, and 2018 May 5, but only two of them are included in this analysis (see Table [1]), as the second XMM-Newton observation (XMM-Newton-b in Table [1]) is heavily contaminated by flares. The two remaining observations, of 5.6 ks and 64.6 ks, respectively, were reduced using the Science Analysis System (SAS; Jansen et al. [2001]) version 19.0.0. In order to remove times when the particle background was high, we inspected the light curve at energies $E > 10$ keV. Then, we chose a value of 0.35 counts s^{-1} for both MOS1 and MOS2, and 0.4 cts s^{-1} for EPIC-PN to remove bright background flares visible in both observations.

For the extraction region, we selected a region of $30''$ for the source and of $40''$ for the background for all the detectors. Considering the multiple X-ray sources (see Figure [1]), we visually inspected the images to avoid any contamination. Finally, we binned the spectra to have at least 15 counts per bin, in order to use the χ^2 statistics.

2.3. NuSTAR Data Reduction

NGC 7479 has been observed by NuSTAR twice, on 2016 March 12 and on 2020 November 6, with an exposure time of $\sim$18 ks and $\sim$23 ks, respectively. The NuSTAR data were retrieved from both focal plane modules, FPMA and FPMB. The event data file was calibrated and cleaned using the NuSTAR nupipeline script version 0.4.8. and the calibration database (CALDB) v.20210427 as a response file. Then, we used the nuproducts script to generate the auxiliary response file, redistribution matrix file, and light-curve files. For both observations, the source spectrum was extracted from a $30''$ circular region centered on the source's optical position. We then extracted the background spectrum from each module, choosing a circular region of $40''$ after a visual inspection to avoid contamination from any other sources. Lastly, the NuSTAR spectra were grouped with the grppha task with a minimum of 15 counts per bin and the χ^2 statistics were used.

3. X-Ray Spectral Analysis

In the following section we describe the different torus models used in the spectral analysis of NGC 7479. The results of this analysis will be shown in Section [4].

To all models, we add a thermal emission component (apec; Smith et al. [2001]) and two emission lines (zgauss), in order to account for the soft X-ray emission from the central region of the host galaxy. A multiplicative constant is added before the apec component (C_{apec}) in order to have a better modulation of the emission between different observations. The absorption along the line of sight due to our Galaxy is taken into account by including the phabs component (4.84×10^{20} cm^{-2}) into the models (Kalberla et al. [2005]). Finally, we model the fraction of the intrinsic AGN power law that is scattered without being reprocessed by the obscuring material, by multiplying the intrinsic power law by the fraction of the scattered emission, F_s.

We apply a multiplicative constant, C_{AGN}, to the intrinsic power-law model, to disentangle intrinsic flux variability from column density variability between the various observations.

We analyzed the torus properties of NGC 7479 by using three models based on Monte Carlo simulations that can self-consistently describe the primary AGN emission with the Compton-thick gas ($N_{H,los} > 1.5 \times 10^{24}$ cm^{-2}) in the surrounding torus. The physical models used in this work are borus02 (Balokovic et al. [2018]), MYTorus (Murphy & Yaqoob [2009]; Yaqoob [2012]; Yaqoob et al. [2015]), and UXCLUMPY (Buchner et al. [2019]).

In XSPEC (Arnaud [1996]) this configuration is as follows:

$$Model = phabs * \{C_{apec} * (apec + zgauss + zgauss)$$
$$+ C_{AGN} * (TorusModel + F_s * pwl)\}. \quad (1)$$

For consistency, we fit all the models in the 0.6–50 keV range. In the simultaneous fitting of all the observations, only C_{AGN} and $N_{H,los}$ are left free to vary between the observations, as we have to take into account possible flux variations and we expect variability in the line-of-sight hydrogen column density. The models' capability to disentangle the line-of-sight column density variability and the intrinsic flux variability is shown in the confidence contour plots (Figure [8]) in Appendix [D]. Other parameters such as the covering factor or the average column density of the torus are instead linked between the observations, as they refer to global torus properties that we do not expect to change over the timescales sampled in this work. As we found the high-energy cutoff to be an unconstrained parameter in our analysis, and in order to be more consistent with recent estimations of its median value ($\sim$300 keV, Baloković et al. [2020]), we froze the high-energy cutoff for all the three models to 300 keV.

3.1. Borus02

The borus02 model assumes a uniform-density sphere with two conical cutouts filled with a cold, neutral, and static medium. The elemental abundance is assumed to be solar apart from the abundance of iron, which is a free parameter. The line-of-sight inclination angle is a variable parameter of the model and it can vary between $\theta \in [18°.2$–$87°.1]$. In this model, the fraction of the sky covered by the torus as seen from the central engine, also known as the covering factor C_F, is left free to vary within the range $C_F \in [0.1$–$1]$; a small value indicates a disklike torus or a nonuniform material distribution, while a large value implies a more spherically symmetric torus. From this we can compute the torus' half-opening angle $\theta_{tor} = \arccos(C_F)$. In addition, borus02 allows the independent calculation of the hydrogen line-of-sight column density ($N_{H,los}$) and the average column density of the torus ($N_{H,av}$).

Since borus02 models only the reflection component of the AGN emission, which accounts for the continuum and the lines, the absorbed and the scattered components need to be added manually.

In XSPEC the model has the following configuration:

$$TorusModel = borus02\_v170323a.fits$$
$$+ zphabs * cabs * cutoffpl, \quad (2)$$

where zpbabs and cabs are the photoelectric absorption due to the cold medium and the Compton scattering losses along the line of sight, respectively.

3.2. MYTorus

The `MYTorus` model considers a cylindrical, azimuthally symmetric torus with a fixed half-opening angle of 60°, filled with a uniform neutral cold reprocessing material. In this model, the main components of an obscured AGN X-ray spectrum (the line of sight, the reflection, and the emission line component) are treated self-consistently by the use of three different tables, as can be seen in Equation (3). In particular, the Compton-scattered and the line components are weighted differently by the addition of multiplicative constants A_S and A_L, respectively.

In this work, we use the decoupled configuration of this model (Yaqoob 2012; Yaqoob et al. 2015), as the coupled configuration (Murphy & Yaqoob 2009) does not allow to disentangle the line-of-sight column density from the average one ($N_{\rm H,av}$). In the decoupled configuration, the zeroth-order continuum (the continuum photons that escaped the torus without being scattered) is independent from the inclination angle, which is fixed to be $\theta_i = 90°$. In this way, the zeroth-order continuum is independent of geometry and it becomes purely a line-of-sight quantity. In order to take into account the possible patchiness and configurations of the torus and of the consequent Compton scattering and line features, these two components are considered both in an edge-on and face-on configuration. In the first case the inclination angle, set to be $\theta_{i,S,L} = 90°$, mimics the forward scattering and it is weighted by $A_{S,L90}$; this means that we are accounting for a more uniform torus, as the photons are primarily reprocessed by the obscuring material that is lying between the AGN and the observer. In the second case, $\theta_{i,S,L} = 0°$ accounts for a backward scattering and $A_{S,L0}$ is the weighting constant. This second scenario is more likely to happen when the torus presents a more patchy structure, in which the photons scattered by the back side of the torus have less chance to interact again with the material before reaching the observer. When $A_{S,L90}$ and $A_{S,L0}$ are left free to vary, we refer at the configuration as "decoupled free" and a ratio between the two constants can give a qualitative idea of which emission is more prominent, thus giving us an indication of the inclination angle of the torus. In addition, a ratio between $N_{\rm H,los}/N_{\rm H,av}$ can give an approximate estimation of the clumpiness of the torus.

In `XSPEC` the model is as follows:

$$TorusModel = \text{mytorus\_Ezero\_v00.fits} * zpowerlw$$
$$+ A_{S,0} * \text{mytorus\_scatteredH300\_v00.fits}$$
$$+ A_{L,0} * \text{mytl\_V000010nEp000H300\_v00.fits}$$
$$+ A_{S,90} * \text{mytorus\_scatteredH300\_v00.fits}$$
$$+ A_{L,90} * \text{mytl\_V000010nEp000H300\_v00.fits}. \quad (3)$$

3.3. UXCLUMPY

`UXCLUMPY` (Buchner et al. 2019) is a physically motivated model constructed to reproduce and model the column density and the cloud eclipsing events in AGN tori in terms of their angular sizes and frequency. In this model, an additional Compton-thick reflector near the corona is added to the model's strong reflection features in a more precise way.

One of the main differences between `UXCLUMPY` and the models described before consists of the inclusion of the clumpiness and the dispersion of the clouds in the model. The model is constructed to reproduce a cloud distribution with different hydrogen column density based on eclipse event rates (Buchner et al. 2019), assuming for the clouds circular Keplerian

orbits on random planes for simplicity. The dispersion of such distribution is modulated by `TORsigma` ($\sigma \in [6°–90°]$), where a large value stands for a large dispersion of the clouds. In some cases, an inner ring of homogeneous gas can be added and modulated by `CTKcover` (C in [0–0.6]); the modeling of the dimension and the extension of the clouds allows to accurately reproduce the reflection hump (see, e.g., Buchner et al. 2019).

The line-of-sight inclination angle $\theta_{\rm inc}$ is left free to vary in the range [0°–90°]. Differently from what is seen in the previous models, `UXCLUMPY` does not allow to distinguish between $N_{\rm H,los}$ and $N_{\rm H,av}$, as the only component taken into account in the model is a total line-of-sight column density that can vary between $N_{\rm H,los} \in [10^{20-26} \text{ cm}^{-2}]$.

In `XSPEC`, the model is as follows:

$$TorusModel = \text{uxclumpy} - \text{cutoff.fits}$$
$$+ F_s^* \text{uxclumpy} - \text{cutoff} - \text{omni.fits}. \quad (4)$$

The first table includes the torus transmitted and reflected component with fluorescent emission lines while the second one, multiplied by the scattering fraction, takes into account the presence of a *warm mirror emitter*, a volume-filling gas between the clumps that is, in part, responsible for the scattering of the intrinsic AGN power law.

4. Results and Discussion

In this section, we present the results of the spectral analysis of NGC 7479. We analyze Chandra and XMM-Newton spectra in the 0.6–8 keV range, while for NuSTAR spectra we select the 3–50 keV range, since the background contribution becomes dominant at higher energies. As mentioned before, we include a thermal component (`apec`) to the physically motivated models in order to better constrain the soft emission of the galaxy[6]; nevertheless our data resolution did not allow us to make further modeling of the gas properties in the galaxy (see, e.g., Torres-Albà et al. 2018). The addition of two Gaussian lines was also required at energies E ~ 0.68 keV and 1.31 keV in order to reproduce the soft-band emission: these line energies are compatible with those of F$K\alpha$1 and Mg $K\beta$1 emission lines. The best-fit values of the simultaneous multi-epoch analysis of NGC 7479 X-ray spectra are shown in Tables 2 and 3, while a more detailed version can be seen in Table 5 in Appendix A. The single-epoch X-ray spectra of NGC 7479 are shown in Appendix C.

4.1. borus02

As already mentioned in Section 3.1, in this model the average column density and the covering factor of the torus are free parameters. To account for the line-of-sight column density, following (Balokovic et al. 2018), we use `zphabs * cabs` to properly measure the Compton scattering. The best-fit values for this model show a $\Gamma = 1.79^{+0.01}_{-0.06}$ and a $N_{\rm H,av} = 17.3^{+30.9}_{-11.7} \times 10^{24} \text{ cm}^{-2}$, both in accordance with what was found by Marchesi et al. (2019). The covering factor is $C_F = 0.88^{+0.01}_{-0.01}$, corresponding to a half-opening angle of the torus $\theta_{\rm tor} = \arccos(C_F) = 28.35^{+1.22}_{-1.19}$, while the inclination angle, left free to vary, results to be $\theta_i = 37.8^{+0.9}_{-0.9}$. The best-fit model and the combined spectra are shown in Figure 2.

---

[6] The thermal component considered here does not take into account multiple gas phases, locations, or temperatures that should be taken into account in order to get a better model of the soft X-ray emission of the host galaxy.

Table 2
X-Ray Fitting Results for NGC 7479

Parameter		borus02	MYTorus Decoupled	UXCLUMPY
stat/dof		476.9/390	480/390	463.9/382
red stat		1.22	1.23	1.21
kT[a]		$0.79^{+0.03}_{-0.03}$	$0.78^{+0.03}_{-0.03}$	$0.80^{+0.02}_{-0.02}$
Γ[b]		$1.79^{+0.01}_{-0.06}$	$1.69^{+0.05}_{-0.10}$	$1.52^{+0.04}_{-0.05}$
$N_{H,av}$[c]		$17.3^{+30.9}_{-11.7}$	$6.03^{+**}_{-1.3}$	...
C_F[d]		$0.88^{+0.01}_{-0.01}$	...	...
$\cos(\theta_i)$[e]		$0.79^{+0.01}_{-0.01}$	...	...
CTKcover[f]		...	...	$0.60^{+**}_{-0.07}$
TORσ[g]		...	...	$24.6^{+20.1}_{-**}$
$A_{S,90}$[h]		...	$0.95^{+0.21}_{-0.15}$	...
$A_{S,0}$[i]		...	$0.32^{+0.13}_{-0.07}$	...
$F_s(\times 10^{-3})$[j]		$0.41^{+0.07}_{-0.07}$	$0.54^{+0.26}_{-0.23}$	$7.06^{+2.80}_{-2.20}$
Norm (10^{-3})[k]		$8.48^{+0.87}_{-0.21}$	$6.07^{+0.13}_{-0.16}$	$2.87^{+0.30}_{-0.30}$
C_{AGN}[l]	XMM-Newton-a	$1.00^{+0.20}_{-0.12}$	$0.95^{+0.29}_{-0.27}$	$0.98^{+0.41}_{-0.44}$
	Chandra-a	$0.60^{+0.19}_{-0.16}$	$0.61^{+0.39}_{-0.30}$	$0.57^{+0.38}_{-0.32}$
	Chandra-b	$0.55^{+0.11}_{-0.09}$	$0.56^{+0.19}_{-0.17}$	$0.53^{+0.27}_{-0.23}$
	NuSTAR-1	1	1	1
	XMM-Newton-c	$1.00^{+0.03}_{-0.07}$	$0.83^{+0.14}_{-0.11}$	$0.86^{+0.28}_{-0.29}$
	NuSTAR-2	$1.00^{+0.07}_{-0.05}$	$0.93^{+0.22}_{-0.18}$	$0.88^{+0.30}_{-0.30}$
$\text{Log}(F_{2,10})$[m]	XMM-Newton-a	$-12.55^{+0.04}_{-0.04}$	$-12.56^{+0.04}_{-0.04}$	$-12.49^{+0.11}_{-0.17}$
	Chandra-a	$-12.57^{+0.10}_{-0.11}$	$-12.57^{+0.10}_{-0.11}$	$-12.56^{+0.17}_{-0.31}$
	Chandra-b	$-12.52^{+0.06}_{-0.06}$	$-12.52^{+0.06}_{-0.06}$	$-12.51^{+0.08}_{-0.11}$
	NuSTAR-1	$-12.65^{+0.03}_{-0.03}$	$-12.61^{+0.03}_{-0.03}$	$-12.45^{+0.08}_{-0.09}$
	XMM-Newton-c	$-12.63^{+0.01}_{-0.01}$	$-12.61^{+0.01}_{-0.01}$	$-12.60^{+0.03}_{-0.04}$
	NuSTAR-2	$-12.64^{+0.02}_{-0.03}$	$-12.62^{+0.02}_{-0.03}$	$-12.47^{+0.05}_{-0.06}$
$\text{Log}(F_{10,40})$[n]	NuSTAR-1	$-11.12^{+0.03}_{-0.03}$	$-11.14^{+0.03}_{-0.03}$	$-11.16^{+0.03}_{-0.04}$
	NuSTAR-2	$-11.06^{+0.02}_{-0.03}$	$-11.07^{+0.03}_{-0.03}$	$-11.11^{+0.03}_{-0.03}$

Notes.
[a] apec model temperature in units of keV.
[b] Power law photon index.
[c] Torus' average hydrogen column density in units of $10^{24}\,\text{cm}^{-2}$.
[d] Covering factor of the torus, as computed using borus02.
[e] Cosine of the inclination angle, as computed using borus02; $\cos(\theta_i) = 0$ represents an edge-on scenario.
[f] Covering factor of the inner ring of clouds, as computed using UXCLUMPY.
[g] Cloud dispersion factor, as computed using UXCLUMPY.
[h] Reflection component constant associated with an edge-on scenario, as computed using MYTorus.
[i] Reflection component constant associated with a face-on scenario, as computed using MYTorus.
[j] Scattering fraction.
[k] Normalization of the intrinsic AGN emission.
[l] Cross-normalization constant between observations; C_{AGN} is fixed to one for NuSTAR observations.
[m] Observed flux between 2 and 10 keV computed using the cflux command.
[n] Observed flux between 10 and 40 keV computed using the cflux command.

4.2. MYTorus Decoupled

As mentioned in Section 3.2, we use the MYTorus model in the *decoupled configuration*, meaning that the constant $A_{S,90}$ and $A_{S,0}$ are left free to vary. The best-fit model and the spectra are
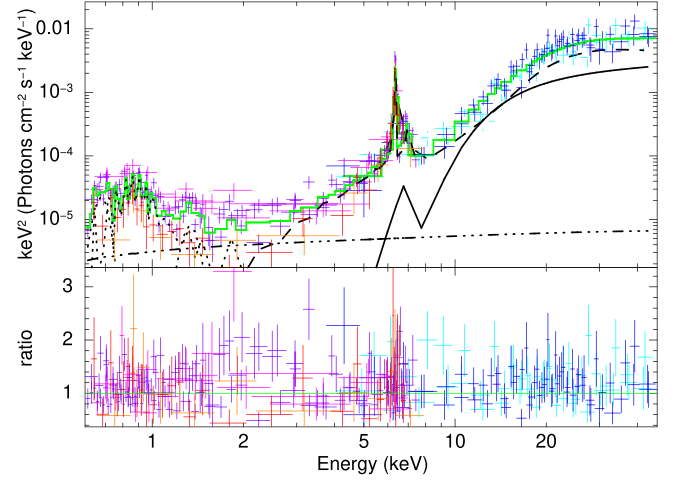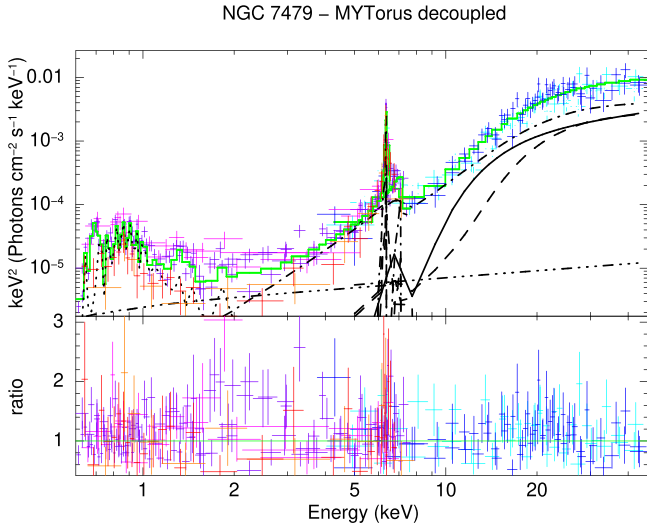

Figure 2. Unfolded Chandra (orange and red), XMM-Newton (purple and magenta), and NuSTAR (blue and cyan) 0.6–50 keV combined spectra of NGC 7479 modeled with borus02. The best-fit model is plotted with a solid green line, while the individual model components are plotted in black. Line-of-sight emission: solid line; reflection component: dashed line; scattering component: dashed–dotted; apec: dotted line.

presented in Figure 3. The best-fit photon index $\Gamma = 1.69^{+0.05}_{-0.10}$ and the $N_{H,av} = 6.0^{+**}_{-1.3} \times 10^{24}\,\text{cm}^{-2}$ are in agreement with the results found by Marchesi et al. (2019). The constants accounting for the intensity of the reprocessed emission component are $A_{S,90} = 0.95^{+0.21}_{-0.15}$ and $A_{S,0} = 0.32^{+0.13}_{-0.07}$, suggesting a forward-reflected dominated scenario, meaning that the majority of the photons scattered toward us pass through the medium between us and the torus. This can point either to an edge-on scenario or to a very large covering factor. These results are in accordance with those obtained using both borus02 and UXCLUMPY (see Sections 4.1 and 4.3).

4.3. UXCLUMPY

The 0.6–50 keV best-fit model is reported in Figure 4. As we were not able to constrain the inclination angle, in order to get consistent results with the previous models and to improve the goodness of the fit (from a reduced statistic of 1.24 to 1.22), we froze the inclination angle to be equal to the one we found using borus02, so $\theta_{i,\text{uxclumpy}} = \theta_{i,\text{borus02}} = 37°.8$. The best-fit photon index is $\Gamma = 1.52^{+0.04}_{-0.05}$; the best-fit value for TORsigma $= 24.6^{+20.1}_{-**}$ and CTKcover $=0.60^{+**}_{-0.07}$ are compatible with a scenario where the AGN has a thick inner ring of Compton-thick cloud in the central region surrounded by thinner clouds dispersed in the outer region of the torus.[7]

4.4. Line-of-sight Hydrogen Column Density Variability Over Time

In Table 3 we report line-of-sight hydrogen best-fit values, as a result of our multiepoch X-ray spectral analysis of NGC 7479; the variability can be visualized in Figure 6. We note that, despite the models being able to provide 90% confidence constraints for $N_{H,\text{los}}$ in almost all model/epoch combinations, parameter confidence contours (see Figures Appendix D) show that the

---

[7] An accurate visualization of this and other distributions of the obscuring material can be found at https://github.com/JohannesBuchner/xars/blob/master/doc/uxclumpy.rst.

Table 3
Line-of-sight Hydrogen Column Density Best-fit Values for NGC 7479 in Units of 10^{24} cm^{-2}

Observation	Date	borus02	MYTorus Decoupled	UXCLUMPY
XMM-Newton-a	2001-06-19	$2.05^{+0.78}_{-0.41}$	$2.00^{+**}_{-0.32}$	$1.75^{+3.21}_{-0.33}$
Chandra-a	2009-08-11	$1.54^{+1.00}_{-0.21}$	$1.50^{+1.00}_{-0.27}$	$1.30^{+2.94}_{-0.28}$
Chandra-b	2009-10-24	$1.40^{+0.18}_{-0.13}$	$1.30^{+0.18}_{-0.13}$	$1.13^{+0.25}_{-0.10}$
NuSTAR-1	2016-05-12	$3.27^{+0.25}_{-0.32}$	$3.99^{+2.44}_{-0.82}$	$3.57^{+0.80}_{-0.57}$
XMM-Newton-c	2018-05-30	$2.40^{+0.28}_{-0.23}$	$2.08^{+0.28}_{-0.17}$	$2.09^{+0.68}_{-0.24}$
NuSTAR-2	2020-11-06	$2.59^{+0.16}_{-0.13}$	$2.77^{+0.38}_{-0.28}$	$2.72^{+0.41}_{-0.38}$

Figure 3. Unfolded Chandra (orange and red), XMM-Newton (purple and magenta), and NuSTAR (blue and cyan) 0.6–50 keV combined spectra of NGC 7479 modeled with MYTorus. The best-fit model is plotted with a solid green line, while the individual model components are plotted in black. Line-of-sight emission: solid line; reflection component: 90° reflection is plotted with dashed line, while the 0° reflection with a dashed–dotted–dashed line; scattering component: dashed–dotted; apec: dotted line.
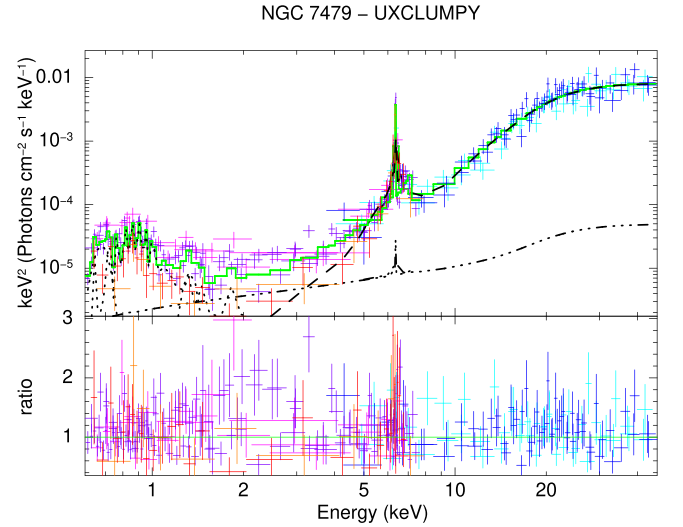
Figure 4. Unfolded Chandra (orange and red), XMM-Newton (purple and magenta), and NuSTAR (blue and cyan) 0.6–50 keV combined spectra of NGC 7479 modeled with UXCLUMPY. The best-fit model is plotted with a solid green line, while the individual model components are plotted in black. Reflection component: dashed line; scattering component: dashed–dotted; apec: dotted line.

degeneracy between $N_{H,los}$ and C_{AGN} is not fully broken in all scenarios. In fact, for the Chandra-a observation we are unable to place upper limits for $N_{H,los}$. By contrast, the degeneracy between $N_{H,los}$—$\cos(\theta_i)$ and $N_{H,los}$—Γ is fully broken for all observations within 1σ (and at 3σ for all but two epochs) as shown in Appendix D.[8]

Interestingly, we notice how the average column density of the torus always remains above the line-of-sight values for both MYTorus and borus02, suggesting a reflection-dominated scenario. We note that the average hydrogen column density of the torus is disentangled from the inclination angle, as shown by the confidence contour plot in Figure 10; *bottom right*. This is in agreement with the high covering factor computed by borus02 ($C_F = 0.88^{+0.01}_{-0.01}$) and the best-fit values found with UXCLUMPY, for which the dispersion of the clouds is TORσ = $24.6^{+20.1}_{-**}$ and the covering factor of the inner reflecting material is CTKcover = $0.60^{+**}_{-0.07}$. This suggests the presence of an inner ring of dense gas (Buchner et al. 2019; Hönig 2019) surrounded by a patchy clumpy torus made of dispersed low-density clouds. This result is in agreement with those obtained by Laha et al. (2020), in where the addition of a partial-cover absorber component is required to model 11/20 of the sources analyzed.
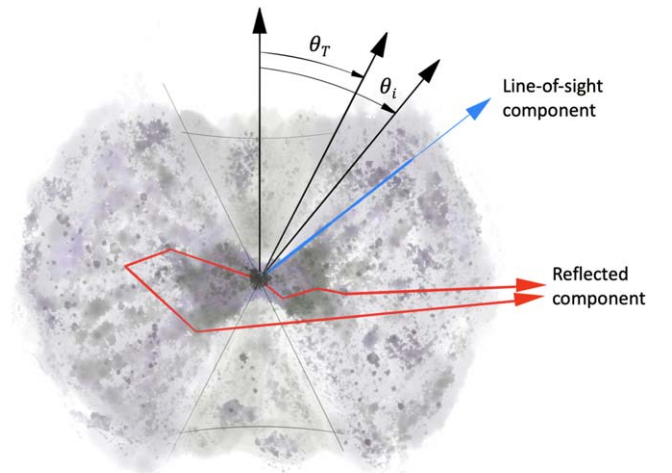

Figure 5. NGC 7479's torus representation based on best-fit parameters obtained during the modeling.

A schematic representation of the torus can be seen in Figure 5. In this case, we used the best-fit data obtained from our analysis (such as covering factor, cloud distribution, and inclination angle) to model what the torus of NGC 7479 would look like, according to our results. This leads us to consider a scenario in which the reflector (i.e., inner ring) and the absorber (i.e., cloud distribution)

---

[8] Considering the good agreement between the three models used in this work, confidence contour plots are shown only for the borus02 model.
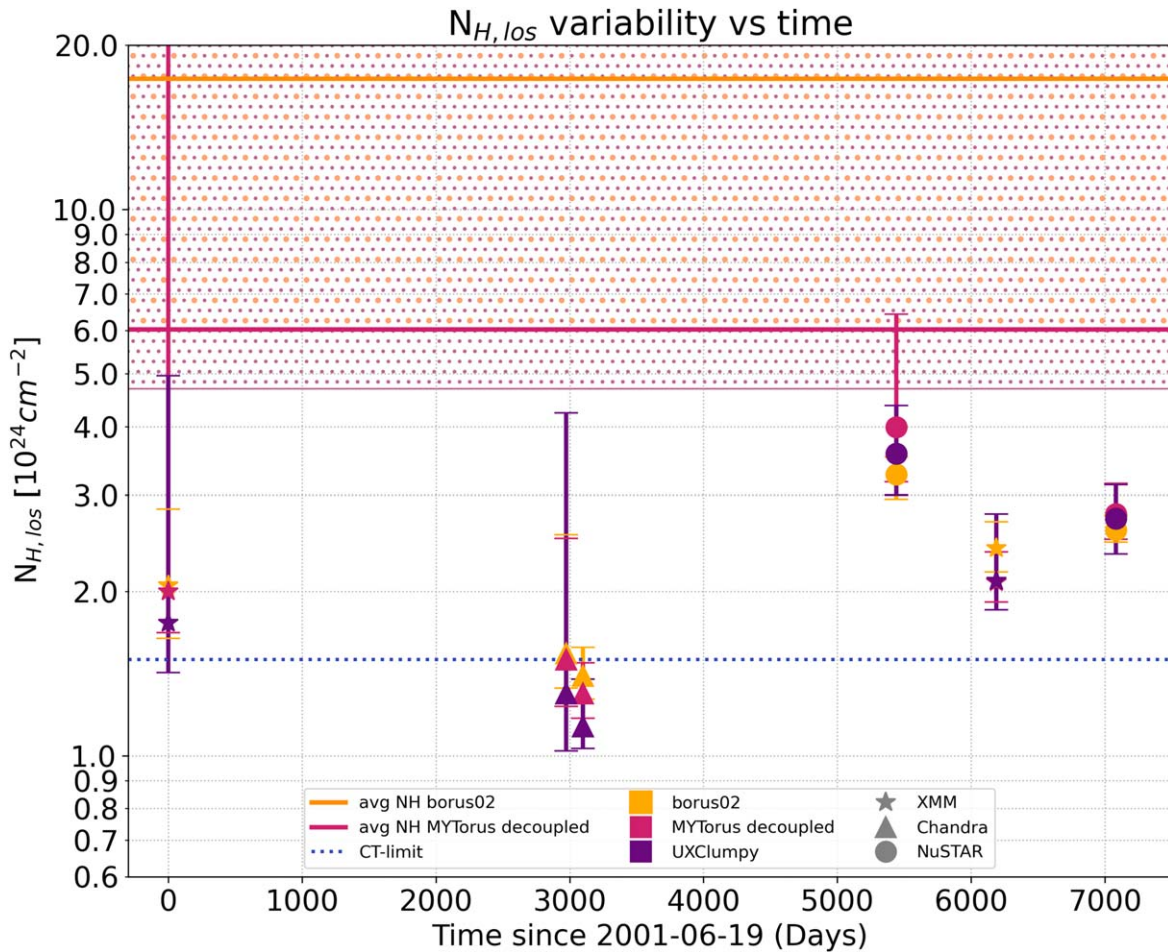
Figure 6. Line-of-sight hydrogen column density variability of NGC 7479 between 2001 and 2020. We note how the $N_{H,av}$ of the torus is higher with respect to the $N_{H,los}$ for all models. For clarity purposes, we added 50 days to the date of the second Chandra observation (Chandra-b in Table 1).

are two different structures within the torus; rather than the whole structure being responsible for both emissions (as often assumed). In this scenario, the inner dense Compton-thick ring generates the reflection-dominated spectra we see in Figures 2, 3, and 4, while the more dispersed clouds, with variable densities, are responsible for the subdominant line-of-sight component. As it can be seen in Figure 6, the variability trend is shown by all the three models, indicating that, despite the reflection-dominated scenario, the quality of the data allows us to confirm a change in the line-of-sight column density.

Using the data we obtained from our $N_{H,los}$ analysis, we compute the upper limit of the cloud distance from the central engine (R), following the approach described in Risaliti et al. (2005). In here, the distance $R \sim 600 t_{100}^2 n_{10}^2 \Delta N_{H,24}^{-2} R_S$ where t_{100} is the variability time in units of 100 ks, $\Delta N_{H,24}$ is the LOS column density difference between two consequent observations in units of 10^{24} cm^{-2} (we can assume it to be the density of the cloud obscuring the central engine during that time), and R_S is the Schwarzschild radius. The cloud density (n_{10}) in units of 10^{10} cm^{-3} can be computed by simply dividing the ΔN_H by the size of the corona, shown to be comprised between $3 R_S$ and $20 R_S$ (Risaliti et al. 2005; Fabian et al. 2015). Using the correlation between stellar velocity dispersion and black hole mass found by Tremaine et al. (2002)[9] and the central stellar

Table 4
Cloud Properties

Observations	ΔNH ($\times 10^{24}$ cm^{-2})	Δt (100 ks)	$D \sim 3R_S$ R (pc)	$D \sim 20R_S$ R (pc)
Chandra-b—NuS-TAR-1	1.87	2.07×10^3	2.37×10^5	5.34×10^3
NuSTAR-1—XMM-Newton-c	0.87	6.64×10^2	2.31×10^4	5.20×10^2

velocity dispersion reported by McElroy (1995), we are able to estimate the mass of the central engine to be $\log(M_{BH}/M_{\odot}) = 7.07$, which is in accordance with the mass computed by Panessa et al. (2006) $\log(M_{BH}/M_{\odot}) = 7.09$, and from here estimate $R_{S,NGC7479} \simeq 3.87 \times 10^{12}$ cm. The results of our calculations are shown in Table 4, where the clouds' distance is reported only when the $N_{H,los}$ between two consecutive observations is not compatible within errors.

Given the general good agreement between the three models used, the values we obtain do not change significantly when each model $N_{H,los}$ is used; for simplicity the distances we report are calculated considering `borus02` $N_{H,los}$ values. What we obtain is an upper limit of the cloud distance, due to the large time window between the observations, in where multiple eclipsing events may have happened. Indeed, only observations

---

[9] The intrinsic scatter of the M_{BH}–σ relation considered is $\epsilon \sim 0.25$–0.30 dex, as reported in Tremaine et al. (2002).

over timescales of days to weeks to months can give a more accurate analysis and vision of the cloud dynamics of NGC 7479 and allow us to better constraint the properties of the obscuration region. Such observations would allow us to better understand the physical differences between the absorber and the reflector, in terms of position and density, as well as their scale.

4.5. Comparison with Previous Results

NGC 7479 was found to be an X-ray CT-AGN candidate by Marchesi et al. (2019) and Zhao et al. (2021) by using XMM-Newton (ObsID 0824450601) and NuSTAR (ObsID 60201037002) observations fitted with the `MYTorus` model and `borus02` in the following configuration ($C_F = 0.5$, $\theta_i = 87°.7$). Although both cases showed the same goodness of fit, they had some discrepancy in the results. Our large data set is able to break the degeneracy model and show that a solution like the one found in Marchesi et al. (2019) is preferred, in where our photon index and average N_H are in perfect agreement within errors. Our best-fit values are also in accordance, within errors, with the ones reported by Tanimoto et al. (2022), where one NuSTAR and one XMM-Newton observation, as well as Swift/XRT data are fitted using the `XClumpy` code (Tanimoto et al. 2019). They find $\Gamma = 1.88^{+0.12}_{-0.16}$ and an average hydrogen column density of $N_{H,av} = 15.3^{+13.5}_{-3.25} \times 10^{24}$ cm^{-2}, both in agreement with our results.

4.6. Bolometric Luminosity, SMBH Mass, and Eddington Ratio

We report the 2–10 keV, 10–40 keV, and 0.6–300 keV intrinsic luminosity of each observation in Table 6 in the Appendix. From here, applying the bolometric correction reported in Vasudevan et al. (2010), we are able to compute the bolometric luminosity of the source, which represents the measurement of the total AGN emission over all electromagnetic energies. Over all epochs, we get a range of $L_{bol} = 4.48$–8.16×10^{43} erg s^{-1}.[10] We can now derive the Eddington luminosity $L_{Edd} = \frac{4\pi G M_{BH} m_p c}{\sigma_T}$, where m_p is the mass of the proton, M_{BH} is the mass of the black hole, and σ_T is the Thompson cross section. Considering the mass we just found, $L_{Edd} = 1.47 \times 10^{45}$ erg s^{-1}. This leads us to the computation of an Eddington ratio range of $\lambda_{Edd} = 0.03$–0.05, where $\lambda_{Edd} = L_{Bol}/L_{Edd}$. This result is in agreement with the value found by Tanimoto et al. (2022) of $\lambda_{Edd} = 0.037$.

The bolometric luminosity can be also derived by adding to the total X-ray luminosity[11] to the far-infrared luminosity of the source (Lusso et al. 2012). From Soifer et al. (2004) we get that $L_{FIR} = 6.35 \times 10^{43}$ erg s^{-1}. Adding this to our total X-ray luminosity we get a range of $L_{bol} = 6.9 - 7.5 \times 10^{43}$ erg s^{-1}, which corresponds to an Eddington ratio range of $\lambda_{Edd} = 0.04$–0.05, in perfect accordance with the previous result we obtained.

5. Conclusions

In this paper we presented the joint fitting of Chandra, XMM-Newton, and NuSTAR observations of NGC 7479, a nearby CT-AGN, using the `borus02`, `MYTorus`, and `UXCLUMPY` models, leading to the following conclusions:

1. The simultaneous multiepoch analysis of NGC 7479 X-ray spectra allowed us to put tight constraints on its torus global properties such the covering factor, the inclination angle, and the average column density.
2. We validate the clumpy torus scenario by measuring the line-of-sight hydrogen column density variability over a time span of ~20 yr. Thanks to such variability, we were able to put an upper limit on the distance of the clouds to the central X-ray emitter.
3. The best-fit parameters suggest the disentanglement of the reflection and the absorption material inside the torus. In particular, the presence of a thick *inner ring* of reflecting medium is required to explain the reflection-dominated spectra.
4. Starting from the X-ray L_{2-10} luminosity, we calculate the bolometric luminosity of $L_{bol} = 4.48$–8.16×10^{43} erg s^{-1} and the Eddington ratio $\lambda_{Edd} = 0.03 - 0.05$ over all epochs for NGC 7479. These are in agreement with what is found in the literature.

Appendix A
X-Ray Fitting Results for NGC 7479

Table 5 reports additional fit parameters for for NGC 7479 not reported in Table 2.

---

[10] For simplicity, we are using the values from our `borus02` best fit.

[11] We measured the luminosity over all the energy ranges taken into account in our best fit.

Table 5
X-Ray Fitting Results for NGC 7479

Parameter		borus02	MYTorus Decoupled	UXCLUMPY
stat/dof		476.9/390	480/390	463.9/382
red stat		1.22	1.23	1.21
kT[a]		$0.79^{+0.03}_{-0.03}$	$0.78^{+0.03}_{-0.03}$	$0.80^{+0.02}_{-0.02}$
C_{apec}[b]	XMM-Newton-a	$0.99^{+0.12}_{-0.12}$	$0.27^{+0.07}_{-0.06}$	$13.60^{+2.78}_{-2.57} \times 10^{-3}$
	Chandra-a	$0.18^{+0.10}_{-0.08}$	$0.05^{+0.03}_{-0.02}$	$2.54^{+1.61}_{-1.27} \times 10^{-3}$
	Chandra-b	$0.31^{+0.07}_{-0.06}$	$0.09^{+0.03}_{-0.02}$	$4.27^{+1.29}_{-1.09} \times 10^{-3}$
	NuSTAR-1	1	1	1
	XMM-Newton-c	$0.66^{+0.03}_{-0.03}$	$0.19^{+0.04}_{-0.03}$	$9.19^{+1.47}_{-1.59} \times 10^{-3}$
	NuSTAR-2	1	1	1
Line 1—Energy		$0.68^{+0.01}_{-0.01}$	$0.69^{+0.01}_{-0.01}$	$0.68^{+0.01}_{-0.02}$
Line 1σ		$0.03^{+0.02}_{-0.02}$	$0.01^{+0.02}_{-**}$	$0.04^{+0.05}_{-0.02}$
Line 1—norm (10^{-5})		$0.84^{+0.54}_{-0.18}$	$2.25^{+1.15}_{-0.65}$	$66.23^{+52.69}_{-18.17}$
Line 2—Energy		$1.33^{+0.03}_{-0.03}$	$1.33^{+0.03}_{-0.03}$	$1.33^{+0.03}_{-0.03}$
Line 2—σ		$0.07^{+0.04}_{-0.03}$	$0.03^{+0.03}_{-0.03}$	$0.06^{+0.04}_{-0.04}$
Line 2—norm (10^{-5})		$0.14^{+0.05}_{-0.05}$	$0.48^{+0.20}_{-0.16}$	$9.19^{+3.28}_{-2.93}$

Notes.
[a] `apec` model temperature in units of keV.
[b] `apec` constant; C_{apec} is fixed to one for NuSTAR observations.

Appendix B
Intrinsic Luminosity of NGC 7479

Table 6 reports the intrinsic luminosity measurements for NGC 7479.

Table 6
Intrinsic Luminosity of NGC 7479 in Units of 10^{42} erg s^{-1}

Parameter	Observation	borus02	MYTorus Decoupled	UXCLUMPY
L_{2-10}	XMM-Newton-a	$4.08^{+0.81}_{-0.49}$	$3.27^{+1.00}_{-0.93}$	$2.09^{+0.89}_{-0.94}$
	Chandra-a	$2.44^{+0.65}_{-0.77}$	$2.10^{+1.34}_{-1.03}$	$1.21^{+0.81}_{-0.68}$
	Chandra-b	$2.24^{+0.36}_{-0.45}$	$1.89^{+0.65}_{-0.59}$	$1.13^{+0.57}_{-0.49}$
	NuSTAR-1	4.08	3.45	2.13
	XMM-Newton-c	$4.08^{+0.12}_{-0.28}$	$2.86^{+0.48}_{-0.38}$	$1.83^{+0.60}_{-0.62}$
	NuSTAR-2	$4.08^{+0.28}_{-0.20}$	$3.20^{+0.75}_{-0.62}$	$1.87^{+0.64}_{-0.64}$
L_{10-40}	NuSTAR-1	4.55	4.73	3.53
	NuSTAR-2	$4.55^{+0.32}_{-0.22}$	$4.40^{+1.04}_{-0.85}$	$3.10^{+1.06}_{-1.06}$

Appendix C
Single-epoch Observations of NGC 7479

Figure 7 reports the single-epochs observation of NGC 7479 modeled with the borus02 model.
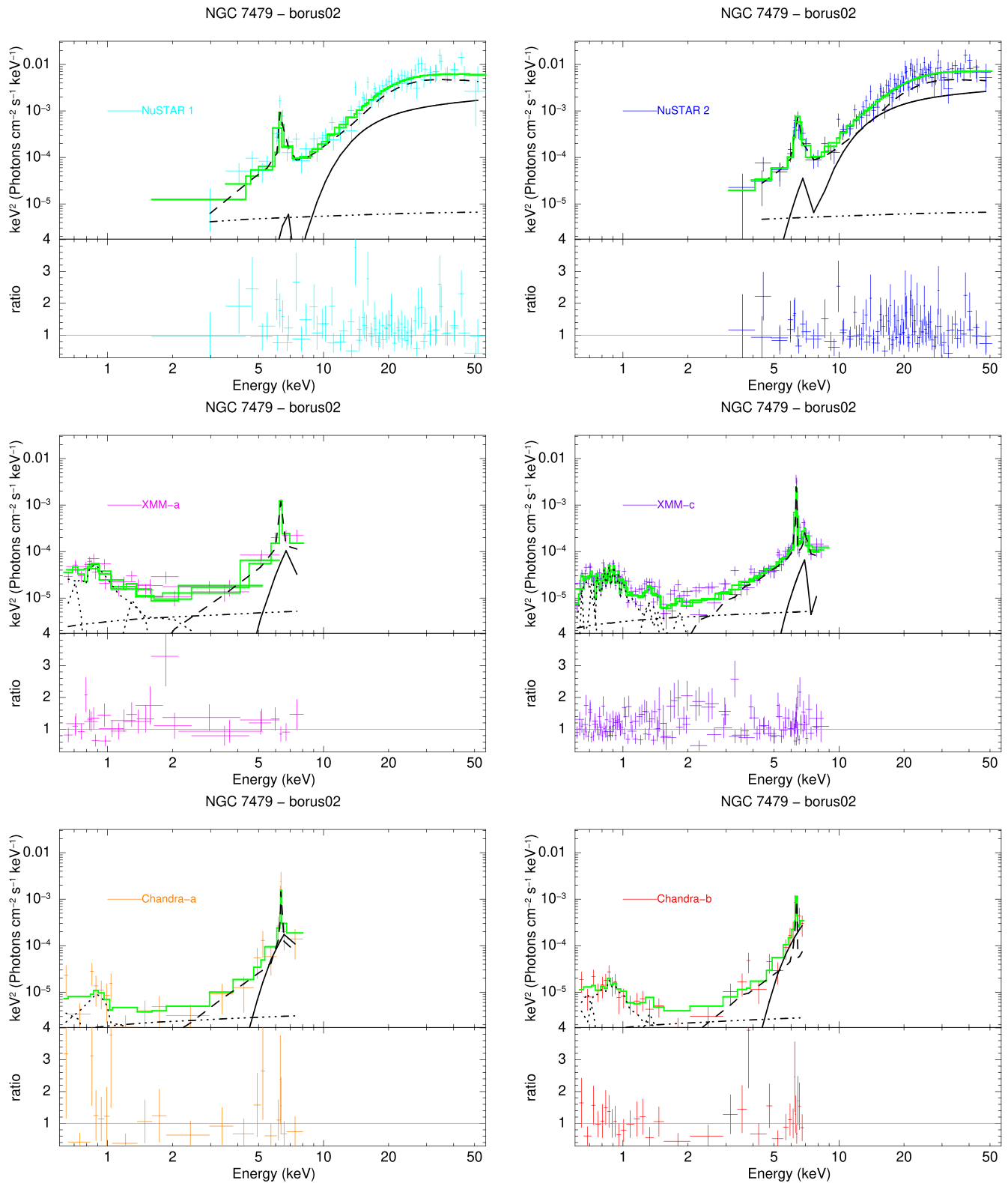

Figure 7. Unfolded NuSTAR (blue and cyan), XMM-Newton (purple and magenta), and Chandra (orange and red) 0.6–50 keV single-epoch spectra of NGC 7479 modeled with borus02. The best-fit model is plotted with a solid green line, while the individual model components are plotted in black. Line-of-sight component: solid line; reflection component: dashed line; scattering component: dashed–dotted; apec: dotted line.

Appendix D
Multidimensional Contour Plots

Figure 8, 9 and 10 report the multidimensional contour plots obtained with the physically motivated models used in this work.
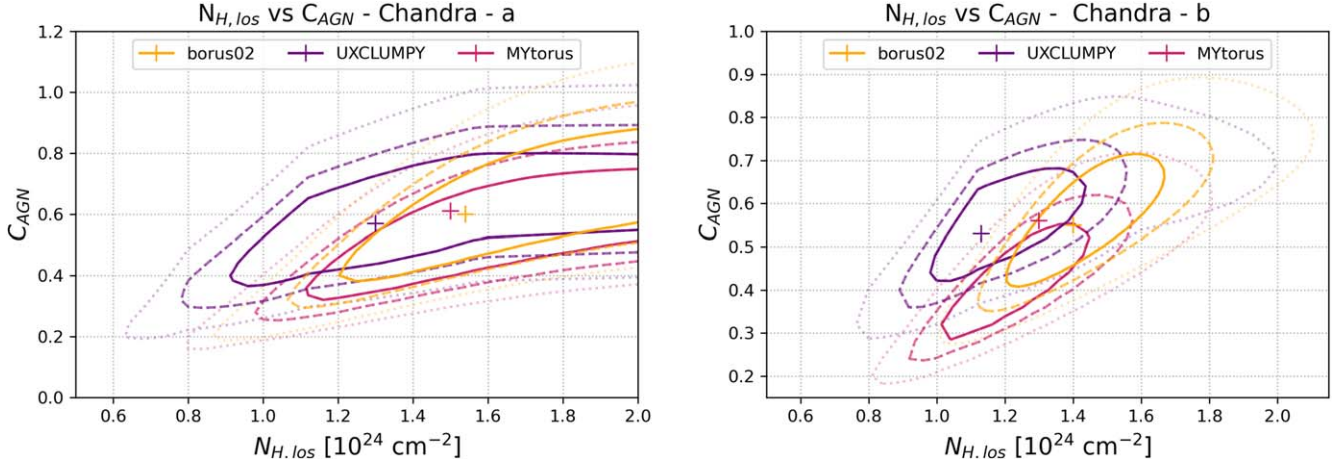

Figure 8. $N_{H,los}$—C_2 multidimensional confidence contour plots for Chandra-a (left), and Chandra-b (right) observations obtained with the three physically motivated models used in this work.
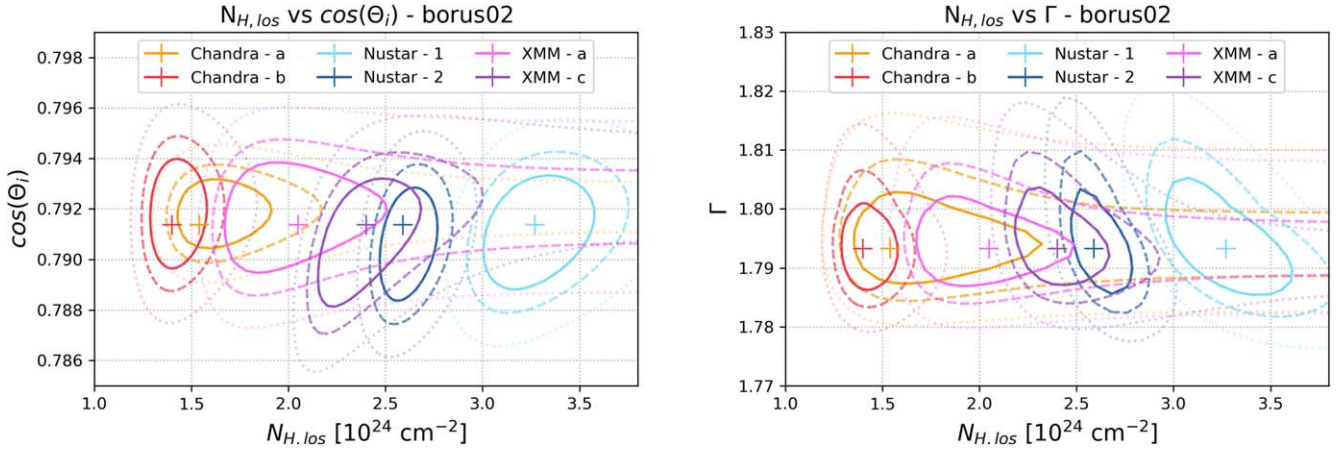

Figure 9. $N_{H,los}$ vs. $\cos\theta_i$, (left), and $N_{H,los}$ vs. Γ (right), multidimensional confidence contour plots obtained with the `borus02` model for all observations. In both cases we see how all parameters are constrained within 1σ.
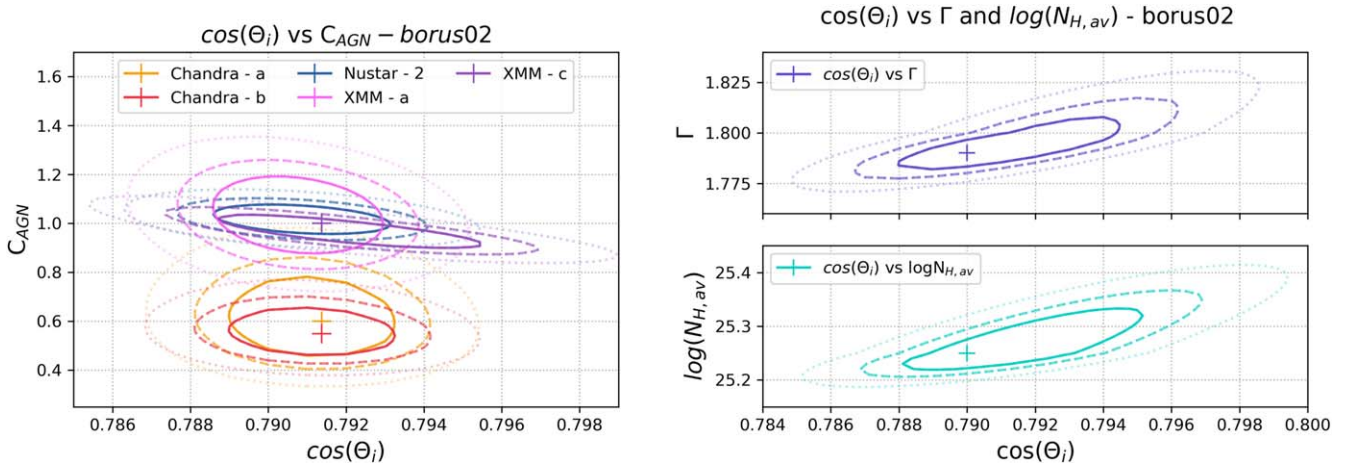

Figure 10. $\cos\theta_i$ vs. C_{AGN} (left), and $\cos\theta_i$ vs. Γ (right—upper) and $\log(N_{H,av})$ (right—bottom) multidimensional confidence contour plots obtained with `borus02` model for all observations. In this case, the degeneracy between the parameters is broken in all scenarios.

ORCID iDs

A. Pizzetti https://orcid.org/0000-0001-6412-2312
N. Torres-Albà https://orcid.org/0000-0003-3638-8943
S. Marchesi https://orcid.org/0000-0001-5544-0749
M. Ajello https://orcid.org/0000-0002-6584-1703
R. Silver https://orcid.org/0000-0001-6564-0517
X. Zhao https://orcid.org/0000-0002-7791-3671

References

Antonucci, R. 1993, ARA&A, 31, 473
Arnaud, K. A. 1996, in ASP Conf. Ser., 101, Astronomical Data Analysis Software and Systems V, ed. G. H. Jacoby & J. Barnes (San Francisco, CA: ASP), 17
Audibert, A., Combes, F., García-Burillo, S., et al. 2019, A&A, 632, A33
Baloković, M., Cabral, S. E., Brenneman, L., & Urry, C. M. 2021, ApJ, 916, 90
Balokovic, M., Brightman, M., Harrison, F. A., et al. 2018, ApJ, 854, 42
Baloković, M., Harrison, F. A., Madejski, G., et al. 2020, ApJ, 905, 41
Bennett, C. L., Larson, D., Weiland, J. L., & Hinshaw, G. 2014, ApJ, 794, 135
Bianchi, S., Guainazzi, M., Matt, G., et al. 2005, A&A, 442, 185
Buchner, J., Brightman, M., Baloković, M., et al. 2021, A&A, 651, A58
Buchner, J., Brightman, M., Nandra, K., Nikutta, R., & Bauer, F. E. 2019, A&A, 629, A16
Cash, W. 1979, ApJ, 228, 939
Combes, F., García-Burillo, S., Casasola, V., et al. 2014, A&A, 565, A97
Combes, F., García-Burillo, S., Audibert, A., et al. 2019, A&A, 623, A79
Elvis, M., Risaliti, G., Nicastro, F., et al. 2004, ApJL, 615, L25
Fabian, A. C., Lohfink, A., Kara, E., et al. 2015, MNRAS, 451, 4375
Fruscione, A., McDowell, J. C., Allen, G. E., et al. 2006, Proc. SPIE, 6270, 62701V
Haynes, M. P., Hogg, D. E., Maddalena, R. J., Roberts, M. S., & van Zee, L. 1998, AJ, 115, 62
Hönig, S. F. 2019, ApJ, 884, 171
Jansen, F., Lumb, D., Altieri, B., et al. 2001, A&A, 365, L1
Kalberla, P. M. W., Burton, W. B., Hartmann, D., et al. 2005, A&A, 440, 775
Kasliwal, M. M., Howell, J. L., Fox, D., Quimby, R., & Gal-Yam, A. 2009, ATel, 2218, 1
Laha, S., Markowitz, A. G., Krumpe, M., et al. 2020, ApJ, 897, 66

Lumsden, S. L., Heisler, C. A., Bailey, J. A., Hough, J. H., & Young, S. 2001, MNRAS, 327, 459
Lusso, E., Comastri, A., Simmons, B. D., et al. 2012, MNRAS, 425, 623
Marchesi, S., Ajello, M., Zhao, X., et al. 2019, ApJ, 872, 8
Markowitz, A. G., Krumpe, M., & Nikutta, R. 2014, MNRAS, 439, 1403
McElroy, D. B. 1995, ApJS, 100, 105
Murphy, Kendrah D., & Yaqoob, Tahir 2009, MNRAS, 397, 1549
Nenkova, M., Sirocky, M. M., Nikutta, R., Ivezić, Ž., & Elitzur, M. 2008, ApJ, 685, 160
Panessa, F., Bassani, L., Cappi, M., et al. 2006, A&A, 455, 173
Pennypacker, C., Perlmutter, S., & Marvin, H. 1990, IAU Circ., 5063, 1
Risaliti, G., Elvis, M., Fabbiano, G., Baldi, A., & Zezas, A. 2005, ApJL, 623, L93
Risaliti, G., Elvis, M., & Nicastro, F. 2002, ApJ, 571, 234
Risaliti, G., Nardini, E., Elvis, M., Brenneman, L., & Salvati, M. 2011, MNRAS, 417, 178
Saha, T., Markowitz, A. G., & Buchner, J. 2022, MNRAS, 509, 5485
Sanfrutos, M., Miniutti, G., Agis-Gonzalez, B., et al. 2013, MNRAS, 436, 1588
Simpson, C. 2005, MNRAS, 360, 565
Smith, R. K., Brickhouse, N. S., Liedahl, D. A., & Raymond, J. C. 2001, ApJL, 556, L91
Soifer, B. T., Neugebauer, G., Matthews, K., Egami, E., & Armus, L. 2004, PASP, 116, 493
Tanimoto, A., Ueda, Y., Odaka, H., et al. 2019, ApJ, 877, 95
Tanimoto, A., Ueda, Y., Odaka, H., Yamada, S., & Ricci, C. 2022, ApJS, 260, 30
Torres-Albà, N., Iwasawa, K., Díaz-Santos, T., et al. 2018, A&A, 620, A140
Tremaine, S., Gebhardt, K., Bender, R., et al. 2002, ApJ, 574, 740
Urry, C. M., & Padovani, P. 1995, PASP, 107, 803
Vasudevan, R. V., Fabian, A. C., Gandhi, P., Winter, L. M., & Mushotzky, R. F. 2010, MNRAS, 402, 1081
Voss, R., Nielsen, M. T. B., Nelemans, G., Fraser, M., & Smartt, S. J. 2011, MNRAS, 418, L124
Yaqoob, T. 2012, MNRAS, 423, 3360
Yaqoob, T., Tatum, M. M., Scholtes, A., Gottlieb, A., & Turner, T. J. 2015, MNRAS, 454, 973
Zhao, X., Marchesi, S., Ajello, M., et al. 2021, A&A, 650, A57
Zhou, Z.-M., Cao, C., Meng, X.-M., & Wu, H. 2011, AJ, 142, 38